Journal of Power Sources 205 (2012) 136–144

Contents lists available at SciVerse ScienceDirect

Journal of Power Sources

journal homepage: www.elsevier.com/locate/jpowsour

Pt nanoparticles supported on mesoporous carbon nanocomposites incorporated with Ni or Co nanoparticles for fuel cells

Fabing Su [a,*], Chee Kok Poh [b], Jianhuang Zeng [c], Ziyi Zhong [b], Zhaolin Liu [d], Jianyi Lin [b]

[a] State Key Laboratory of Multiphase Complex Systems, Institute of Process Engineering, Chinese Academy of Sciences, Beijing 100190, China
[b] Institute of Chemical Engineering and Sciences, A*star, 1 Pesek Road, Jurong Island, Singapore 627833, Singapore
[c] School of Chemistry and Chemical Engineering, South China University of Technology, Guangzhou 510641, China
[d] Institute of Materials Research and Engineering of Singapore, A*star, 3 Research Link, Singapore 117602, Singapore

ARTICLE INFO

Article history:
Received 28 October 2011
Received in revised form
27 December 2011
Accepted 1 January 2012
Available online 10 January 2012

Keywords:
Mesoporous carbon nanocomposites
Pt catalyst
Electrochemical catalysis
Characterization
Fuel cells

ABSTRACT

We report the preparation and characterization of mesoporous carbon nanocomposites with Ni and Co nanoparticles incorporated into the pore walls, which are synthesized via template strategy by sucrose-impregnation and benzene chemical vapor deposition (CVD) routes separately. Pt nanoparticles supported on the nanocomposites for oxygen reduction reaction (ORR) and methanol oxidation reaction (MOR) in fuel cells are fabricated via hydrogen reduction method. It is found that the introduction of metal nanoparticles into the pore walls of carbon materials via both synthesis routes had negligible change in pore structure. Highly dispersed Pt nanoparticles supported on nanocomposites synthesized by sucrose-impregnation method shows better catalytic activities for both ORR and MOR than that on those by CVD method and greatly improve the limiting current densities for ORR. The promotional effect of Ni on the catalytic activity of Pt catalysts for both ORR and MOR is evidenced in nanocomposites obtained with sucrose-impregnation method, but not with CVD method. Interesting results revealed that Ni performed as a better promoter in MOR while Co is a better promoter in ORR. Our investigation not only provides further insight on the roles of Ni and Co in ORR and MOR, but also can assist the design and synthesis of the new nanostructured electrocatalyst supports.

1. Introduction

It is well known that there are a number of technical problems in the commercial application of proton exchange membrane fuel cells (PEMFCs) and direct methanol fuel cells (DMFCs), e.g., sluggish anodic methanol oxidation reaction (MOR) in DMFCs and cathodic oxygen reduction reaction (ORR) on Pt electrocatalysts, and the high cost of noble metal Pt used [1], which should be addressed and overcome. The discovery of new electrocatalyst materials with high efficiency and low cost thus is imperative. Currently, the strategies adopted to improve the catalytic performance and cost-efficiency include further improving Pt-based electrocatalysts [2], developing better catalyst carbon supports [3,4], and searching alternative non-platinum active metal [5]. Although non-Pt catalysts look attractive [6], so far Pt is still widely accepted as the standard catalyst for the oxidation of small organic molecules in fuel cells. However, the catalytic activity of monometallic Pt catalysts is still not good enough for the large-scale application of fuel cells. Therefore, in recent years, catalysts consisting of Pt nanoparticles coupled with transitional metals such as Co, Ni, and Fe have been tested to improve the electrocatalytic activity in both MOR and ORR [7,8]. These include for mechanically alloyed PtCo and PtNi electrocatalysts [9], core-shell PtCo nanocrystals [10], nano-structured Pt–Fe/C [11], Pt monolayer deposited on core-shell nanoparticles (Pt/Au/Ni, Pt/Pd/Co, and Pt/Pt/Co) [12] and porous Pd–Cu alloys [13], core-shell Pd/FePt nanoparticles [14], Ni@Pt core-shell nanoparticles [15], carbon-supported Pt–Co catalysts [16–19], dealloyed Pt–Cu–Co nanoparticles [20]. Some of them showed much better electrochemical performance than the state-of-the-art commercial Pt/C electrocatalysts. The investigation of the dissociation behavior of O_2 on Pt–Co and Pt–Fe alloys indicated that, for ORR, alleviation of poisoning and enhanced rates for reactions involving O is because of the presence of more active Pt skins derived from introduction of Co and Fe [21,22]. Recent research has found tuning the surface electronic structure of Pt via metals (Ni, Co, Fe, and Ti) is substantially responsible for the high activity of electrocatalysts for ORR [2,23,24].

Template strategy has been used to prepare novel nanostructured carbon materials [4,25–29], in particular, to obtain the carbon–metal composites for electrocatalysts [30–33]. Such nanocomposites could allow allocation of the metal nanoparticles within their well-defined carbon pore walls [34], resulting

* Corresponding author. Tel.: +86 10 82544850; fax: +86 10 82544851.
E-mail address: fbsu@mail.ipe.ac.cn (F. Su).

0378-7753/$ – see front matter © 2012 Elsevier B.V. All rights reserved.
doi:10.1016/j.jpowsour.2012.01.050

in high dispersion of metal nanoparticles in carbon support matrixes [31,32], ameliorating metal–support contact and interaction between Pt and second metal phase, as well as tailoring their sizes for understanding the catalytic mechanism. Our previous reports showed that the Pt nanoparticles supported on sandwiched Ru/carbon nanocomposites exhibited an improved activity [35]. Moreover, such catalyst nanostructure with predefined allocation of active metal nanoparticles within the support matrix would possibly allow us to design nanostructured catalysts for much better catalytic behaviors.

Herein, we comparatively investigate the effects of Ni and Co nanoparticles incorporated in carbon matrixes on the electrochemical properties of Pt catalysts in MOR and ORR. The introduction of Ni and Co within the templated carbon pore walls was conducted via sucrose-impregnation and chemical vapor deposition (CVD) methods. Pt nanoparticles are deposited on these nanocomposites to form bimetallic catalysts by conventional impregnation followed by hydrogen reduction at a mild temperature. The investigation of effects of these metal–carbon nanocomposites on the electrochemical activities of catalysts for MOR and ORR will give an insight into the role of transitional metals and nanostructured electrocatalyst supports.

2. Experimental

2.1. Materials synthesis

Ordered mesoporous carbon (*OMC*): OMC was synthesized using sucrose-impregnation method as reported previously [36]. Briefly, 1.0 g of SBA-15 was first added to a solution containing 1.3 g of sucrose, 0.13 g of H_2SO_4, and 4.0 mL of H_2O. The mixture was dried in an oven at 100 °C for 6 h and subsequently at 150 °C for 6 h. Then, the obtained sample was added in a solution containing 0.8 g of sucrose, 0.08 g of H_2SO_4, and 3.0 mL of H_2O, and dried again at 120 °C for 6 h. The dried sample was carbonized at 900 °C for 3 h in nitrogen gas. Finally, the black sample was treated with a 10% HF solution to remove silica template, washed with deionized water, subsequently dried at 120 °C overnight, and assigned as OMC.

Ordered mesoporous carbon synthesized by CVD method (*OMCV*): OMCV was prepared using CVD method [26]. Briefly, around 1.0 g of pure silica SBA-15 template was placed in a crucible and loaded in a horizontal quartz tube located in a furnace. The temperature was then raised up to 900 °C in highly pure N_2 flow (30 cm^3 min^{-1}) with a heating rate of 5 °C min^{-1}. Subsequently, a N_2 flow (50 cm^3 min^{-1}) containing benzene vapor generated from a liquid bubbler was passed through the quartz tube. After the CVD reaction of benzene occurred at 900 °C for 3 h, the sample was cooled in pure nitrogen to obtain a silica/carbon composite. The silica template was removed using a 10% HF solution at room temperature for 24 h, followed by washing with copious deionized water and dried in air at 120 °C overnight to yield a carbon sample, which was denoted as OMCV.

CoOMC and CoOMCV: 0.20 g of cobalt nitrate hexahydrate ($Co(NO_3)_2{\cdot}6H_2O$, Sigma–Aldrich, 98%) was dissolved into 6.0 mL of deionized water, then mixed with 2.0 g of silica SBA-15, and further dried in air at 200 °C for 3 h to form a metal–silica composite. The composite was employed as the template instead of pure silica via sucrose-impregnation route mentioned above to obtain Co ordered mesoporous carbon containing Co and denoted as CoOMC, while that obtained with CVD route was named CoOMCV.

NiOMC and NiOMCV: 0.20 g of cobalt nitrate hexahydrate ($Ni(NO_3)_2{\cdot}6H_2O$, Sigma–Aldrich, 98%) was dissolved into 6.0 mL of deionized water and then mixed with 2.0 g of silica SBA-15. Later, the mixture was dried in air at 200 °C for 3 h to generate Ni–silica composite. NiOMC and NiOMCV were prepared the method similar to synthesis of CoOMC and CoOMCV.

Pt catalysts: Using OMC, OMCV, CoOMC, CoOMCV, NiOMC, and NiOMCV nanocomposites as the supports, Pt catalysts including Pt/OMC, Pt/OMCV, Pt/CoOMC, Pt/CoOMCV, Pt/NiOMC, and Pt/NiOMCV, were prepared with the incipient wet impregnation method, respectively. In brief, 0.10 g of support was first mixed with a 0.30 mL solution containing 0.07 g chloroplatinic acid hydrate ($H_2PtCl_6{\cdot}xH_2O$, ~38 wt.% Pt, Aldrich). The resultant mixture was kept in air at 80 °C overnight and then at 150 °C for 3 h. Subsequently, the solid products were heated at 400 °C for 2 h with a ramp of 2 °C min^{-1} in a mixed atmosphere containing argon (40 mL min^{-1}) and hydrogen (10 mL min^{-1}), and then washed with hot deionized water for five times to remove residual chlorine ions in catalysts. After that, the solid was vacuum-dried at 80 °C overnight.

2.2. Characterization

The porous properties of the samples were investigated using physical adsorption of nitrogen at the liquid-nitrogen temperature on an automatic volumetric sorption analyzer (Quantachrome, AUTOSORB 6B). Prior to the measurement, the samples were degassed under vacuum at 200 °C overnight. The specific surface areas were determined according to the Brunauer–Emmett–Teller (BET) method in the relative pressure range of 0.05–0.2. The total pore volumes were obtained from the volume of nitrogen adsorbed at the relative pressure of 0.99. Pore size distribution (PSD) curves were derived from the Barrett–Joyner–Halenda (BJH) method using the adsorption branches. The pore sizes were estimated from the maximum positions of the BJH PSD curves. The X-ray diffraction (XRD) patterns in the Bragg's angle (2θ) range from 10° to 90° were collected on a Bruker D8 diffractometer with Cu Kα radiation of wavelength $\lambda = 0.1541$ nm for identification of the crystalline structure and average crystallite size of Pt particles. Thermogravimetric analysis (TGA) was conducted on a thermogravimetric analyzer TGA Q500 (Thermal Analysis Instruments, U.S.A.) in air with a flow rate of 100 mL min^{-1} and a temperature ramp of 10 °C min^{-1}. The microscopic features of the samples were observed with a transmission electron microscope (TEM) (Tecnai G^2 TF20 S-twin, FEI Company) operated at 200 kV. The surface chemical composition of the samples was determined by X-ray photoelectron spectroscopy (XPS) on a VG ESCALAB 250 spectrometer (Thermo Electron, U.K.), using a non-monochromatized Al Kα X-ray source (1486 eV).

A three-compartment electrochemical cell was used to evaluate the electrochemical performances of the catalysts by cyclic voltammetry (CV) at room temperature. An Autolab PGSTAT302 served as the potentiostat/galvansotat. The working electrode was fabricated by casting Nafion-impregnated catalyst ink onto a 5 mm diameter vitreous glassy carbon disk electrode. 4.0 mg of Pt catalyst was ultrasonically dispersed into 2.0 mL of 2-propanol containing Nafion solution (5 wt.%, DuPont) for 30 min to form a catalyst ink; 10 μL of the catalyst ink was dropped on the disk using a micropipette and then the catalyst-coated electrode was dried in a vacuum oven at 80 °C for 30 min. A flat Pt sheet and an Ag/AgCl electrode were used as the counter and reference electrode respectively. High purity nitrogen gas was bubbled into the electrolyte to purge the oxygen before measurement. All reported potentials were referenced to the standard hydrogen electrode (SHE). The catalysts were electrochemically cleaned by continuous cycling until a stable response was obtained before the cyclic voltammograms were recorded. Oxygen reduction reaction measurement was conducted in a 0.5 M H_2SO_4 aqueous electrolyte saturated with oxygen and a disk rotation rate of 2000 rpm. Methanol oxidation reaction was carried out in the 0.5 M H_2SO_4 and 1.0 M CH_3OH aqueous electrolyte.

Table 1
Physicochemical properties of the supports.

Sample	S_{BET} [a] ($m^2\ g^{-1}$)	V_t [b] ($cm^3\ g^{-1}$)	D^c (nm)	MOx[d] (wt.%)
OMC	1150	1.27	3.9	–
OMCV	815	0.86	3.8	–
CoOMC	1176	1.09	3.7	3.7
CoOMCV	965	0.95	3.7	7.7
NiOMC	1221	1.18	3.7	3.6
NiOMCV	785	0.85	3.5	7.5

[a] BET surface area.
[b] Total pore volume at the relative pressure of 0.99.
[c] Pore size derived from BJH method of adsorption branch.
[d] Metal content within supports derived from TG analysis.

3. Results and discussion

3.1. Characterization of supports

Fig. 1 shows the nitrogen adsorption/desorption isotherms and BJH–PSD curves of the support samples. It can be seen that the isotherms of all nanocomposites displayed a type-IV isotherm with a H2 hysteresis loop, indicative of mesoporous materials [37]. In the relative pressure range of 0.4–0.7, a steep capillary condensation step can be seen from adsorption and desorption branches in Fig. 1a, indicating the presence of relatively uniform mesopores. The narrow peaks in PSD curves of Fig. 1b derived from adsorption branch were centered at the pore size of 3.9 nm and 3.8 nm for OMC and OMCV respectively, whereas CoOMC, CoOMCV, and NiOMC showed a pore size of 3.7 nm. The centered pore size of NiOMCV is at around 3.5 nm. Table 1 compiles the physicochemical properties of supports. The BET surface areas are comparable for supports prepared by sucrose-impregnation method (OMC: 1150 $m^2\ g^{-1}$, CoOMC: 1176 $m^2\ g^{-1}$, and NiOMC: 1221 $m^2\ g^{-1}$); nanocomposites prepared by CVD method also have comparable BET surface area (OMCV: 815 $m^2\ g^{-1}$, CoOMCV: 965 $m^2\ g^{-1}$, and NiOMCV: 785 $m^2\ g^{-1}$). Their pore volumes also have similar trend. Nanocomposites prepared by CVD method have lower BET surface area and pore volume than those prepared by impregnation method possibly due to the higher graphitic nature of the former. These results suggest that the incorporation of Co and Ni has negligible effects on the pore structure of the obtained nanocomposites.

Fig. 2 shows the XRD patterns of the supports. It can be seen that for all samples there are two diffraction peaks at 2θ values of around 25° and 43°, which can be assigned to (0 0 2) and (1 0 1) planes of the carbon material, respectively. The (0 0 2) peak of supports prepared by sucrose-impregnation method (CoOMC, NiOMC, and OMC) is much weaker and broader than that of the samples obtained by CVD

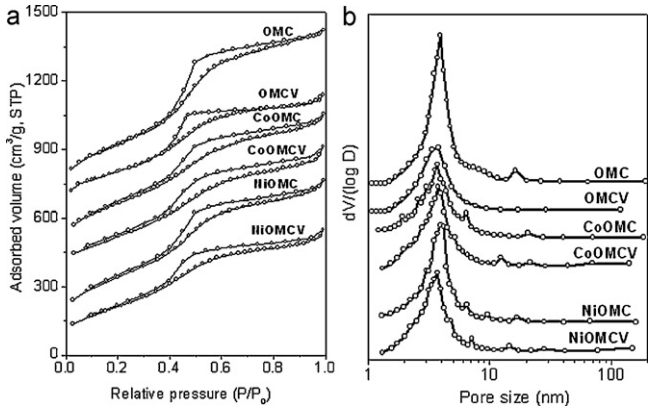

Fig. 1. (a) Adsorption–desorption isotherms of the nanocomposites (for clarity, the isotherms of OMC, OMCV, CoOMC, and CoOMCV were vertically shifted for 600, 600, 350, and 300 $cm^3\ g^{-1}$, respectively), and (b) BJH–PSD curves of all nanocomposites.

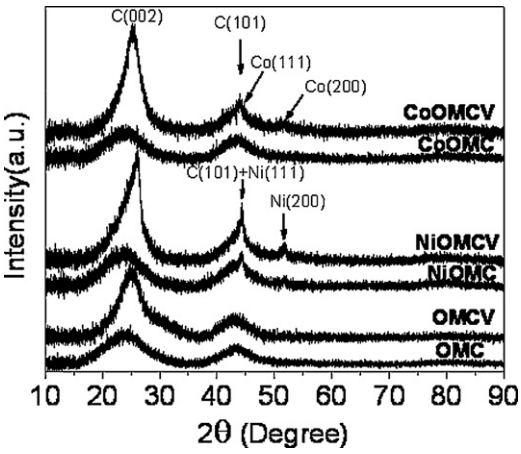

Fig. 2. XRD patterns of the nanocomposites.

route (OMCV, CoOMCV and NiOMCV), indicating the lower graphite crystallinity of the former samples. Moreover, their peak positions of the CVD prepared samples shift to a higher angle, from 23.6° of OMC versus 25.1° of OMCV, 24.5° of NiOMC versus 26.1° of NiOMCV, and 23.6° of CoOMC versus 25.2° of CoOMCV, implying the shorter distance between graphite layers of the supports synthesized by CVD method. These results suggest that the CVD method could result in higher graphitic degree of carbon supports compared to those prepared by the traditional impregnation-carbonization route. In addition, for NiOMC and NiOMCV samples, two peaks at 44.5° and 51.9° corresponding to (1 1 1) and (2 0 0) reflections respectively, can be indexed to a face-centered cubic (fcc) structure of nickel (JCPDS file No. 4-485) same as previous report [38]. It is noted that the irregularity of the peak at about 44.5° is due to peak overlap of the (1 0 1) reflection of carbon and the (1 1 1) reflection of Ni metal. XRD pattern of CoOMCV shows that the very low intensity peaks observed at 44.5° and 52.5° corresponds to (1 1 1) and (2 0 0) diffractions, respectively, indicating the presence of small fcc-Co particles [38]. However, no Co peaks were found for CoOMC, suggesting that the Co nanoparticles are too small to be detected as shown in below TEM image.

TEM images of the supports are shown in Fig. 3. All images are taken along [0 0 1] directions for better observation. Images of OMC in Fig. 3a and OMCV in Fig. 3b show highly ordered structure with an interplanar distance of around 10 nm. A thicker carbon layer on the external surface of OMCV can be seen from Fig. 1b, which was formed because of the prolonged CVD time. Such nonporous carbon layer would be partially responsible for the low surface area and pore volume than that of OMC as shown by the data in Table 1. Images of NiOMC in Fig. 3c and NiOMCV also show highly ordered array of pore structure. For NiOMC, no Ni nanoparticles are clearly observed, but for NiOMCV, large black dots, Ni particles, can be seen in Fig. 3d, suggesting that NiOMC possesses a much higher dispersion and smaller size of Ni particles compared with NiOMCV, which is in good agreement with above XRD analysis. Our previous reports have shown that the ordered mesoporous structure of OMC could be retained after incorporation of metal nanoparticles [39,40]. Similarly, CoOMC in Fig. 3e and CoOMCV in Fig. 3f also show highly aligned pore channels and Co particles in the former is much smaller and more highly dispersed in the carbon matrix. The result suggests that the sucrose-impregnation method would lead to the high dispersion of metal nanoparticles within the carbon walls [31,32].

Fig. 4 shows the TG curves of various supports. The residual weight for OMC and OMCV is almost zero at 800 °C, indicative of complete oxidation of the carbon supports and sufficient removal of the silica template by HF solution. TG curves for NiOMC and CoOMC

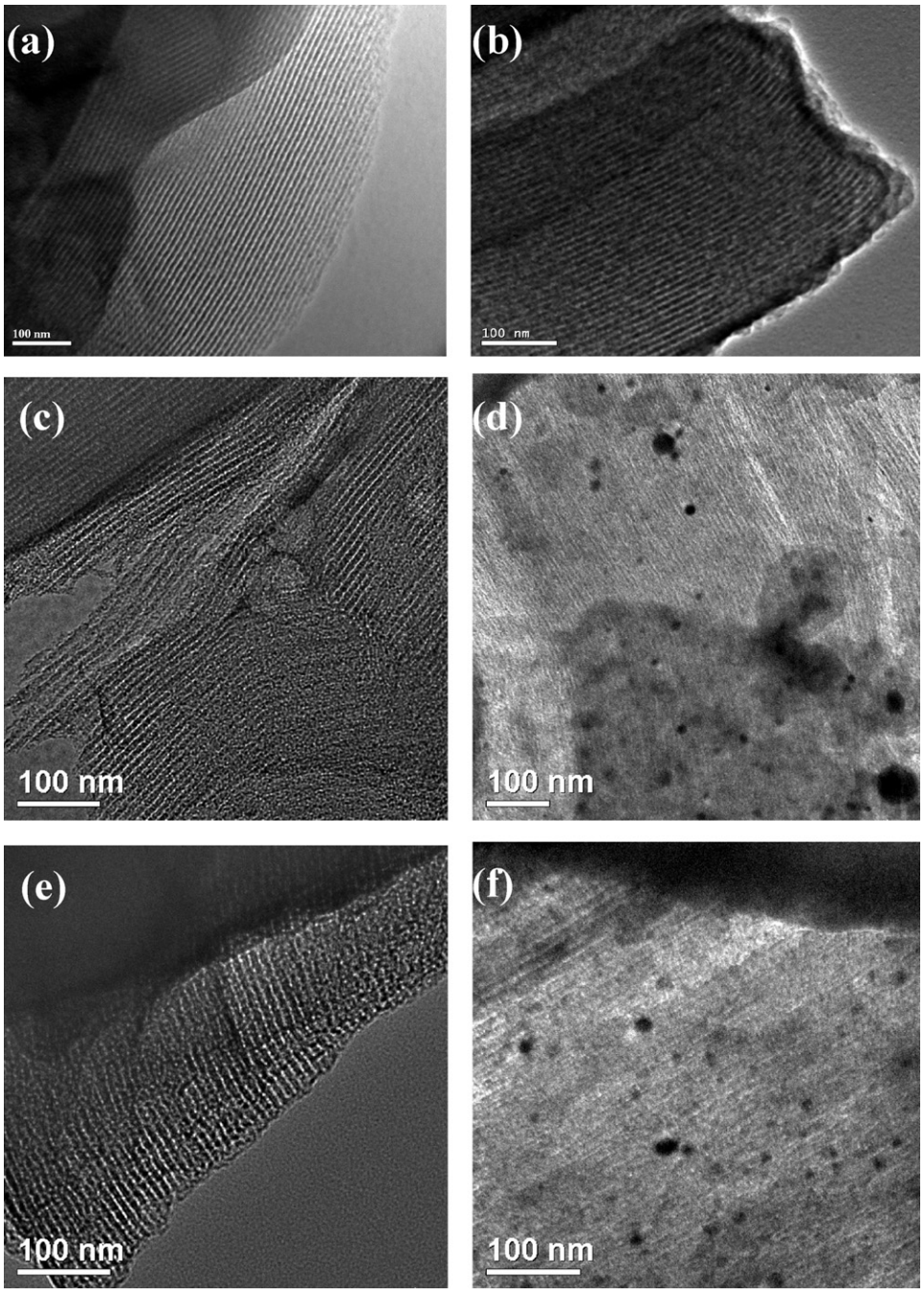

Fig. 3. TEM images: (a) OMC, (b) OMCV, (c) NiOMC, (d) NiOMCV, (e) CoOMC, and (f) CoOMCV.

are almost identical, with a residual weight of about 3.7 wt.%, attributed to NiO or CoO, respectively. The weight remnant for CoOMCV and NiOMCV is around 7.7 wt.%. The temperature at which the major weight loss occurred for CoOMCV and NiOMCV is higher than that for CoOMC and NiOMC. This is possibly due to their high thermal stability since both of them have a higher graphitic degree caused via CVD, which was confirmed by above XRD and TEM observation.

3.2. Characterization of Pt catalysts

Fig. 5 shows the TG plots of Pt catalysts supported on all supports. Complete oxidization of carbon took place at temperature over 600 °C and the major weight loss occurs in the temperature range from 420 to 470 °C for all catalysts. The residual weight is 19.6 wt.% for Pt/OMC and Pt/OMCV, 24.1 wt.% for Pt/CoOMC and Pt/NiOMC, and 26.8 wt.% for Pt/CoOMCV and Pt/NiOMCV. Since the metal oxide content for NiOMC and CoOMC in Fig. 4 is 3.7 wt.%, Pt loading in Pt/CoOMC and Pt/NiOMC can be calculated to be 20.4 wt.%. Similarly, the Pt loading in Pt/CoOMCV and Pt/NiOMCV can be derived to be 19.2 wt.%. All catalysts, therefore, have comparable Pt loadings, at around 20.0 wt.%. The weight loss for all the catalysts in Fig. 5 mainly occurred at a lower temperature than that of supports in Fig. 4, probably due to the Pt catalytic oxidation effect.

Fig. 6 shows the XRD patterns of the catalysts. The diffraction peaks at the Bragg angles of around 39°, 46°, 67° and 81° in Fig. 6a correspond to the (1 1 1), (2 0 0), (2 2 0) and (3 1 1) facets of face centered cubic Pt nanocrystals [41]. The peaks originated from Ni

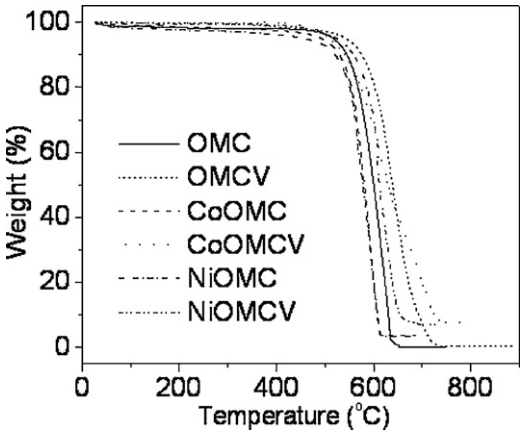

Fig. 4. TG curves of the nanocomposites.

and Co are not observed due to their much weaker signals and also, they are not alloyed with Pt nanoparticles regardless of the methods used. Fig. 6b shows the zoomed view of the diffraction peaks at (2 2 0), in which, Pt (2 2 0) peaks for Pt/OMC, Pt/CoOMC and Pt/NiOMC catalysts have lower intensity and broader full width at half-maximum (FWHM) compared to their counterparts (Pt/OMCV, Pt/CoOMCV and Pt/NiOMCV), indicative of relatively smaller particle sizes for former catalysts on supports derived from sucrose-impregnation method. The average Pt crystallite size was calculated from the Pt (2 2 0) peak using Scherrer equation. It can be seen that the particle size of Pt on supports from sucrose-impregnation is much smaller than that obtained via CVD method, where it is 8.9 nm for Pt/OMC versus 12.1 nm for Pt/OMCV, 10.6 nm for Pt/CoOMC versus 13.2 nm for Pt/CoOMCV, 11.5 nm for Pt/NiOMC versus 15.6 nm for Pt/NiOMCV.

Fig. 7 reveals the TEM images of the Pt catalysts, in which, Pt nanoparticles are homogenously dispersed in the pores of all the supports. Pt particles supported on the nanocomposites prepared by CVD method are relatively bigger than those on the nanocomposites made by the sucrose-impregnation method, which is agreement with the above XRD observation. It is observed that there is no agglomeration of Pt nanoparticles occurred for all catalysts and most Pt nanoparticles are located in the pores although the average Pt particle size is much larger than that of pore channels of supports. This size 'mismatch' may be explained by the localized destruction of carbon during the metal nanoparticles formation, which has been used for cutting carbon nanotubes [42]. The high dispersion of Pt nanoparticles on supports is attributed to the high surface area of supports and the constricted growth within the

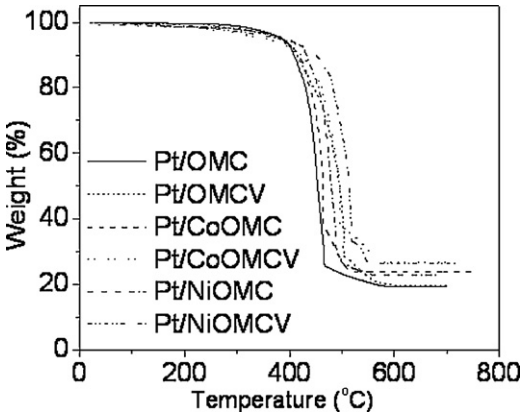

Fig. 5. TG plots of Pt catalysts.

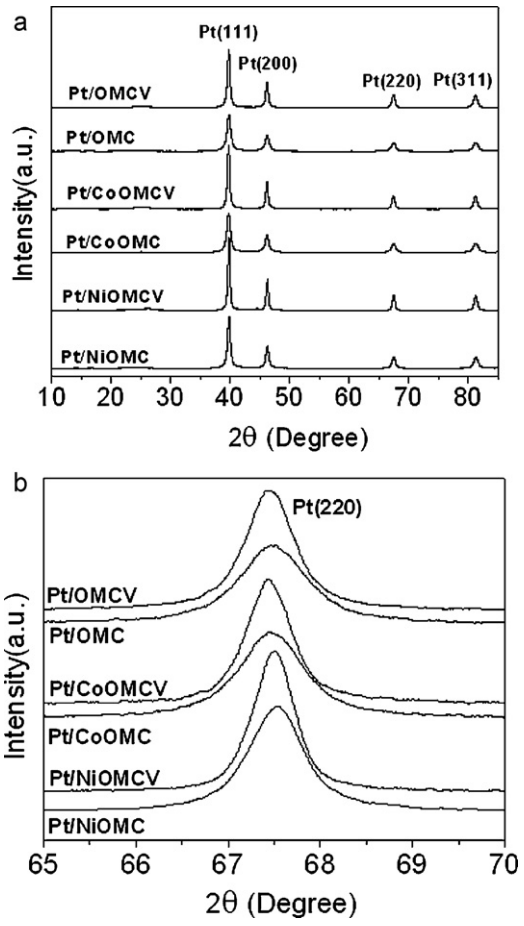

Fig. 6. XRD patterns of Pt catalysts: (a) wide angle, (b) zoomed view of the Pt (2 2 0) diffraction peak.

well-developed mesopores, which could prevent Pt nanoparticles from aggregating during H_2 reduction treatment.

Fig. 8 presents the Pt4f spectra of catalyst samples. Each spectrum can be deconvoluted into three pairs of doublets labeled with I–III [43]. The most intense doublet with BE of 71.3 eV ($Pt4f_{7/2}$) and 74.5 eV ($Pt4f_{5/2}$) is attributed to metallic Pt, while the peaks at around 72.2 and 75.5 eV can be assigned to Pt^{2+} chemical state as in either PtO or $Pt(OH)_2$ [44]. The third pair of peaks at about 74.2 and 77.5 eV is ascribed to Pt^{4+} species on the Pt particles surface, such as PtO_2 [45,46]. These Pt oxide species may be due to oxygen chemisorption at the step and kink sites present on the Pt surface [47]. The integration of peak areas indicates that most Pt species exist as metallic Pt for all the catalysts. The stronger intensity of Pt4f peaks for Pt on the nanocomposites derived from sucrose-impregnation route than from CVD indicates, in the former sample, the more Pt particles are deposited on the pore surface, and they have stronger interaction with O-containing surface functional groups of the nanocomposites [48], consistent with the above pore structure and XRD analysis, in which nanocomposites derived from sucrose-impregnation route have a higher surface area and are amorphous. Additionally, the signals from Ni and Co are very weak (not shown here), suggesting these nanoparticles are mostly buried in the carbon matrix.

3.3. Electrochemical performance of Pt electrocatalysts

In order to compare the catalytic activities of the catalysts, current densities reported in this work are all normalized to the Pt loading. Fig. 9a shows the CV curves for the catalysts. The catalysts

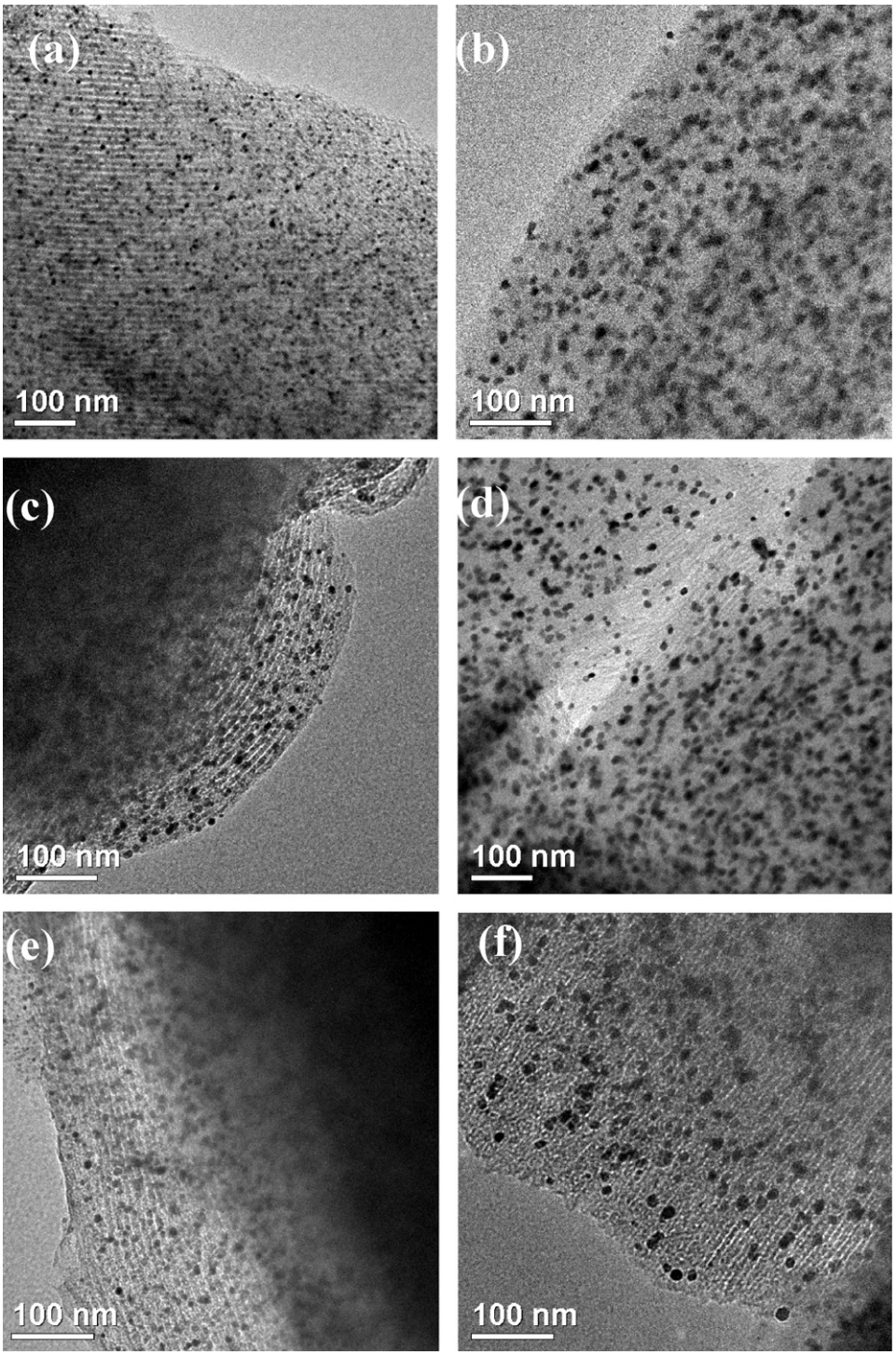

Fig. 7. TEM images: (a) Pt/OMC, (b) Pt/OMCV, (c) Pt/NiOMC, (d) Pt/NiOMCV, (e) Pt/CoOMC, and (f) Pt/CoOMCV.

are cycled between −0.2 V and 1.2 V in 0.5 M H_2SO_4 at room temperature with a scan rate of 100 mV s^{-1}. A pair oxidation/reduction peak was found between 0.4 V and 0.6 V for all the catalysts, which could arise from the remnant quinine-like surface species on the carbon support. Considerable capacitive charges can be seen on all the catalysts in the total range of scan. Strong underpotential hydrogen adsorption and desorption sites are observed for all catalysts except for Pt/CoOMCV and Pt/NiOMCV in the potential region smaller than 0.06 V (vs. SHE). This is due to the fact that Pt/CoOMCV and Pt/NiOMCV have significantly larger Pt particle size, which are 13.2 nm and 15.6 nm respectively and thus the catalysts are lack of adsorption sites for hydrogen ions. The voltammograms of Pt/CoOMCV and Pt/NiOMCV clearly shows that from 0.06 V to 0.27 V in the hydrogen desorption region, there is a featureless and flat current plateau which is an indication of the existence of Pt (1 1 1) terrace sites on the catalysts [49]. These show that the Pt deposited on CoOMCV and NiOMCV mainly forms Pt crystallite films which consist of Pt (1 1 1) surface. CV curve of Pt/OMCV shows obvious Pt (1 1 0) desorption peak at 0.116 V and another desorption peak at 0.246 V which is contributed by Pt (1 0 0) step sites on Pt (1 1 1)

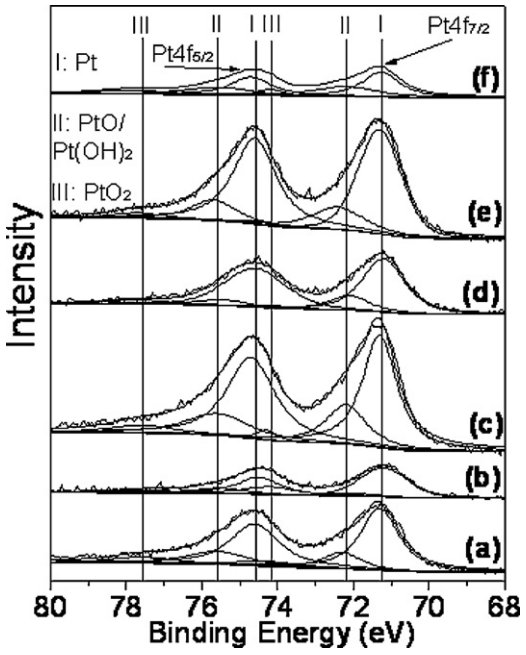

Fig. 8. XPS spectra of Pt4f: (a) Pt/OMC, (b) Pt/OMCV, (c) Pt/CoOMC, (d) Pt/CoOMCV, (e) Pt/NiOMC, and (f) Pt/NiOMCV.

domain [49], which clearly indicates that Pt particles supported on OMCV are polycrystalline nanoparticles. Pt/NiOMC, Pt/OMC and Pt/CoOMC also show similar features.

Fig. 9b shows the specific mass activities for MOR as measured by CV in 0.5 M CH_3OH + 0.5 M H_2SO_4 at a scan rate of 20 mV s^{-1} at room temperature. The MOR activity, the highest current density evaluated at around 0.85 V, was 110.3 mA mg^{-1} for Pt/NiOMC, 102.1 mA mg^{-1} for Pt/CoC, 93.9 mA mg^{-1} for Pt/OMC, 82.7 mA mg^{-1} for Pt/OMCV, 58.4 mA mg^{-1} for Pt/NiOMCV, and 52.1 mA mg^{-1} for Pt/CoOMCV respectively, following the order of: Pt/NiOMC > Pt/CoOMC > Pt/OMC > Pt/OMCV > Pt/NiOMCV > Pt/CoOMCV. Generally, the addition of Ni and Co to carbon supports derived via sucrose-impregnation method enhanced the MOR activity and Pt/NiOMC registered the highest activity. On the contrary, incorporation of Ni and Co in supports fabricated by CVD method had negative effects, which are evidenced by the lower activity of Pt/NiOMCV and Pt/CoOMCV than that of Pt/OMCV.

Fig. 9c shows the ORR mass activity of the catalysts. The polarization curves are obtained in the electrolytes of 0.5 M H_2SO_4 at a scan rate of 5 mV s^{-1} and room temperature. The ORR activities of the catalysts as indicated by the current density in the Tafel region (0.85–0.75 V vs. SHE) from high to low, are arranged in the following order: Pt/OMCV > Pt/CoOMC > Pt/NiOMC ≈ Pt/OMC > Pt/NiOMCV > Pt/CoOMCV.

A quantitative approach for the evaluation of the ORR activities of the catalysts can be obtained through the number of electrons transferred per O_2 molecules (n) which was calculated from the Koutecky–Levich (K–L) equation [50].

$$\frac{1}{I} = \frac{1}{I_k} + \frac{1}{I_d} = \frac{1}{\eta FAkC^b_{O_2}} + \frac{1}{0.62nFAD^{2/3}_{O_2}\nu^{-1/6}C^b_{O_2}\omega^{1/2}} \quad (1)$$

where I is the measured current; I_k and I_d are the kinetic and diffusion-limited currents, respectively. F is the Faraday constant; A is the electrode area; k is the electrochemical rate constant for O_2 reduction; $C^b_{O_2}$ (1.1×10^{-6} mol cm^{-3}) is the bulk concentration of O_2; D_{O_2} (1.4×10^{-5} cm^2 s^{-1}) is the oxygen diffusivity, and ν (1×10^{-2} cm^2 s^{-1}) is the kinetic viscosity of the electrolyte (0.5 M H_2SO_4). Fig. 10a shows the K–L plot for the

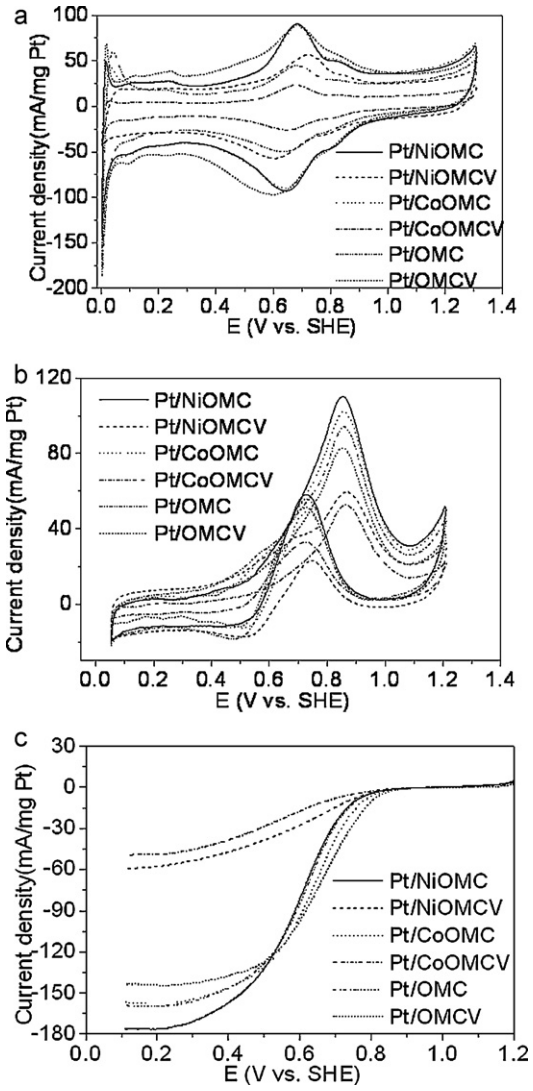

Fig. 9. (a) CV plots of catalysts measured in the electrolytes of 0.5 M H_2SO_4 at room temperature at a scan rate of 100 mV s^{-1}, (b) CV curves of catalysts measured in the electrolyte of 0.5 M H_2SO_4 + 1 M CH_3OH at a scan rate of 20 mV s^{-1} at room temperature, and (c) ORR activity on catalysts in electrolytes of 0.5 M H_2SO_4 saturated with O_2 (rotation rate = 2000 rpm, sweep rate = 5 mV s^{-1}, room temperature).

catalysts at 0.7 V (vs. SHE). The number of electrons transferred per O_2 molecules (n) were calculated for the Pt/OMCV (n = 3.88), Pt/CoOMC (n = 3.62), Pt/NiOMC (n = 3.40), Pt/OMC (n = 3.39), Pt/NiOMCV (n = 1.73), and Pt/CoOMCV (n = 1.59). The order of the catalysts, arranged according to the number of electrons transferred per O_2 molecules (n) from high to low is Pt/OMCV > Pt/CoOMC > Pt/NiOMC ≳ Pt/OMC > Pt/NiOMCV > Pt/CoOMCV, identical to the conclusion from the ORR plot. Fig. 10b shows the electrons transfer process occurred at different potential. At potential larger than 0.6 V (vs. SHE), all catalysts completed the overall four-electron ORR except for Pt/NiOMCV and Pt/CoOMCV where their kinetics are sluggish due to the fact that larger Pt (1 1 1) domain formed by the Pt deposited on OMCV as observed in the CV curves. The analysis using K–L equation is consistent with the observation in the Tafel region of the ORR plot. Apart from the Tafel region in the ORR plot, we observed that the limiting current densities for the metal catalyst supported on OMC are generally larger than the catalysts with OMCV as support. Higher limiting current densities of OMC supported catalysts compared to OMCV supported catalysts might be due to the fact that OMCV were formed under high temperature decomposition of hydrocarbon and thus OMCV has

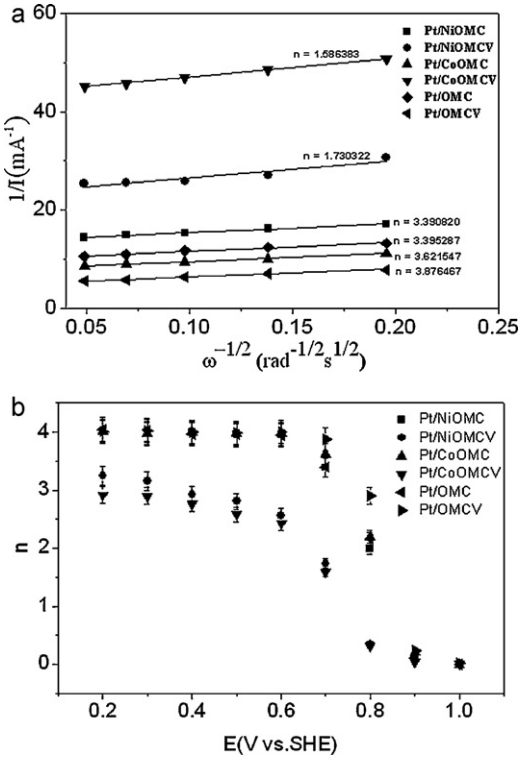

Fig. 10. K–L plots for the catalysts at 0.7 V (vs. SHE), and (b) electron transfer process occurred at different potentials.

higher graphitization and lower porosity as indicated by the BET results, and thus lead to poorer mass transport of reactant while the synthesis procedure of OMC lead to the opposite results and hence better mass transport of O_2. Obviously, the limited current densities for Pt/CoOMCV and Pt/NiOMCV are the lowest among all catalysts, this might be due to the fact that Co is a better catalyst than Ni for graphitization of carbon atoms, thus the porosity of the OMCV is even lower for Co doped OMCV than Ni doped OMCV. The limiting current density for Pt/CoOMC, Pt/OMC and Pt/NiOMC is at 157, 159 and 176 mA mg^{-1} Pt respectively, indicating that the turnover of ORR reaction is the highest for Pt/NiOMC. This is because the incorporation of foreign atoms in the OMC created disorder in the carbon matrix, and also due to larger molecule of sucrose, the effect of graphitization of carbon by the metal catalyst (Ni) is not significant hence NiOMC (S_{BET} = 1221 m^2 g^{-1}) and is more porous than OMC (S_{BET} = 1150 m^2 g^{-1}) and lead to significantly larger limiting current density for Pt/NiOMC. Since Co is a better catalyst for graphitization of carbon, the effect of disorder created by foreign atoms was cancelled out by the catalyzing effect and hence lead to a similar BET surface area (S_{BET} = 1176 m^2 g^{-1}) and limiting current density (157 mA mg^{-1} Pt).

From the ORR evaluation, we found that incorporation of Ni and Co changes the ORR performances of the catalysts. In general, doping of Ni and Co in OMC improves the performance of catalyst supported by OMC, while incorporation of Ni and Co in OMCV has negative effect on the catalysts supported by OMCV. Apart from the effect on the porosity of OMC and OMCV, the doping of Ni and Co also affects the structure and activity of the Pt nanoparticles deposited on OMC and OMCV. As we mentioned, Pt deposited on NiOMCV and CoOMCV formed larger Pt (1 1 1) domains that reduced the performance of the catalysts, due to the catalyzing effect by Ni and Co for carbon graphitization, OMCV become less porous and hence larger Pt particles were formed during the deposition step. On the other hand, Pt deposited onto NiOMC and CoOMC show improvement over Pt supported by undoped OMC in ORR. This improvement in ORR activity might come from the enhancement of electronic charge transfer with the incorporation of Co and Ni atoms.

As for methanol oxidation, catalysts with OMC as support performed better than catalysts supported by OMCV. This is because larger porosity is more crucial for methanol oxidation since methanol molecules are larger than O_2 molecules. Doping of Ni in OMC further increased the porosity of OMC, and also enhanced the electronic charge transfer of OMC. The enhancement in the electronic charge transfer is more significant in methanol oxidation since the overall reaction of methanol oxidation is a six-electron process as given by the equation below:

$$CH_3OH + H_2O \Leftrightarrow CO_2 + 6H^+ + 6e^- \quad (2)$$

We can conclude that doping of Ni and Co into OMC and OMCV supports not only changes the physical structures but also the electronic charge transfer properties of the final catalysts. However the details on how Ni and Co dopants affect the charge transfer properties is still unclear. Further investigation should be carried out to understand the mechanism behind this and to improve the overall catalyst activity in both ORR and MOR.

4. Conclusions

Ordered mesoporous metal–carbon nanocomposites with incorporation of Ni and Co nanoparticles are prepared using Co and Ni deposited ordered mesoporous silica SBA-15 as hard templates, respectively. The carbon precursors are introduced via two routes, namely the sucrose-impregnation method and CVD method. The nanocomposites synthesized by former method include ordered mesoporous carbon (OMC), Ni-doped OMC (NiOMC), and Co-doped OMC (CoOMC), while the nanocomposites OMCV, NiOMCV, and CoOMCV are prepared by later method. It is found that the sucrose-impregnation method leads to the formation of OMC, NiOMC, and CoOMC nanocomposites with higher surface area and more defects than OMCV, NiOMCV, and CoOMCV, respectively. As a result, the Pt nanoparticles are more easily deposited on the OMC, NiOMC, and CoOMC, and have smaller sizes compared to OMCV, NiOMCV, and CoOMCV, respectively. The ORR activity at the Tafel region from highest to lowest follows in the order: Pt/OMCV > Pt/CoOMC > Pt/NiOMC ≈ Pt/OMC > Pt/NiOMCV > Pt/CoOMCV, while the MOR activity follows the order: Pt/NiOMC > Pt/CoOMC > Pt/OMC > Pt/OMCV > Pt/NiOMCV > Pt/CoOMCV. Clearly, the Pt nanoparticles deposited on the carbon supports synthesized by the sucrose-impregnation method show better catalytic activity than those on the supports from CVD. Furthermore, the incorporation of Ni within carbon matrix via sucrose-impregnation method can promote the catalytic activity of Pt nanoparticles in both reactions. The work would be helpful for understanding the role of transitional metals (Ni and Co) and for generating new nanostructured electrocatalyst supports.

Acknowledgments

Financial supports from Hundred Talents Program of the Chinese Academy of Sciences, National Natural Science Foundation of China (No. 21031005), State Key Laboratory of Multiphase Complex Systems, and Scientific Research Foundation for the Returned Overseas Chinese Scholars (State Education Ministry) are gratefully acknowledged.

References

[1] A. Ermete, Mater. Chem. Phys. 78 (2003) 563–573.
[2] V.R. Stamenkovic, B. Fowler, B.S. Mun, G. Wang, P.N. Ross, C.A. Lucas, N.M. Markovic, Science 315 (2007) 493–497.

[3] A.L. Dicks, J. Power Sources 156 (2006) 128–141.
[4] S.H. Joo, S.J. Choi, I. Oh, J. Kwak, Z. Liu, O. Terasaki, R. Ryoo, Nature 412 (2001) 169–172.
[5] R. Bashyam, P. Zelenay, Nature 443 (2006) 63–66.
[6] K. Gong, F. Du, Z. Xia, M. Durstock, L. Dai, Science 323 (2009) 760–764.
[7] E. Antolini, J.R.C. Salgado, E.R. Gonzalez, J. Power Sources 160 (2006) 957–968.
[8] Y. Bing, H. Liu, L. Zhang, D. Ghosh, J. Zhang, Chem. Soc. Rev. 39 (2010) 2184–2202.
[9] M.A. García-Contreras, S.M. Fernández-Valverde, J.R. Vargas-García, M.A. Cortés-Jácome, J.A. Toledo-Antonio, C. Ángeles-Chavez, Int. J. Hydrogen Energy 33 (2008) 6672–6680.
[10] N.S. Sobal, U. Ebels, H. Mohwald, M. Giersig, J. Phys. Chem. B 107 (2003) 7351–7354.
[11] W. Li, W. Zhou, H. Li, Z. Zhou, B. Zhou, G. Sun, Q. Xin, Electrochim. Acta 49 (2004) 1045–1055.
[12] J. Zhang, F.H.B. Lima, M.H. Shao, K. Sasaki, J.X. Wang, J. Hanson, R.R. Adzic, J. Phys. Chem. B 109 (2005) 22701–22704.
[13] M. Shao, K. Shoemaker, A. Peles, K. Kaneko, L. Protsailo, J. Am. Chem. Soc. 132 (2010) 9253–9255.
[14] V. Mazumder, M. Chi, K.L. More, S. Sun, J. Am. Chem. Soc. 132 (2010) 7848–7849.
[15] Y. Chen, F. Yang, Y. Dai, W. Wang, S. Chen, J. Phys. Chem. C 112 (2008) 1645–1649.
[16] E.I. Santiago, L.C. Varanda, H.M. Villullas, J. Phys. Chem. C 111 (2007) 3146–3151.
[17] P. Yu, M. Pemberton, P. Plasse, J. Power Sources 144 (2005) 11–20.
[18] J.H. Zeng, J.Y. Lee, J. Power Sources 140 (2005) 268–273.
[19] Y. Qian, W. Wen, P.A. Adcock, Z. Jiang, N. Hakim, M.S. Saha, S. Mukerjee, J. Phys. Chem. C 112 (2008) 1146–1157.
[20] R. Srivastava, P. Mani, N. Hahn, P. Strasser, Angew. Chem. Int. Ed. 46 (2007) 8988–8991.
[21] Y. Xu, A.V. Ruban, M. Mavrikakis, J. Am. Chem. Soc. 126 (2004) 4717–4725.
[22] S. Chen, P.J. Ferreira, W. Sheng, N. Yabuuchi, L.F. Allard, S.-H. Yang, J. Am. Chem. Soc. 130 (2008) 13818–13819.
[23] S. Vojislav, S.M. Bongjin, J.J.M. Karl, N.R. Philip, M.M. Nenad, R. Jan, G. Jeff, K.N. Jens, Angew. Chem. Int. Ed. 45 (2006) 2897–2901.
[24] Z.B. Wang, P.J. Zuo, G.J. Wang, C.Y. Du, G.P. Yin, J. Phys. Chem. C 112 (2008) 6582–6587.
[25] R.J. White, V. Budarin, R. Luque, J.H. Clark, D.J. Macquarrie, Chem. Soc. Rev. 38 (2009) 3401–3418.
[26] F. Su, J.H. Zeng, X. Bao, Y. Yu, J.Y. Lee, X.S. Zhao, Chem. Mater. 17 (2005) 3960–3967.
[27] Z. Lei, S. Bai, Y. Xiao, L. Dang, L. An, G. Zhang, Q. Xu, J. Phys. Chem. C 112 (2008) 722–731.
[28] G. Zhao, J. He, C. Zhang, J. Zhou, X. Chen, T. Wang, J. Phys. Chem. C 112 (2008) 1028–1033.
[29] A. Stein, Z. Wang, M.A. Fierke, Adv. Mater. 21 (2009) 265–293.
[30] W.C. Choi, S.I. Woo, M.K. Jeon, J.M. Sohn, M.R. Kim, H.J. Jeon, Adv. Mater. 17 (2005) 446–451.
[31] S.-H. Liu, R.-F. Lu, S.-J. Huang, A.-Y. Lo, S.-H. Chien, S.-B. Liu, Chem. Commun. (2006) 3435–3437.
[32] S.-H. Liu, W.-Y. Yu, C.-H. Chen, A.-Y. Lo, B.-J. Hwang, S.-H. Chien, S.-B. Liu, Chem. Mater. 20 (2008) 1622–1628.
[33] Z. Wen, J. Liu, J. Li, Adv. Mater. 20 (2008) 743–747.
[34] H.H.M. Fröba, Carbon 45 (2007) 304–314.
[35] J. Zeng, F. Su, Y.-F. Han, Z. Tian, C.K. Poh, Z. Liu, J. Lin, J.Y. Lee, X.S. Zhao, J. Phys. Chem. C 112 (2008) 15908–15914.
[36] S. Jun, S.H. Joo, R. Ryoo, M. Kruk, M. Jaroniec, Z. Liu, T. Ohsuna, O. Terasaki, J. Am. Chem. Soc. 122 (2000) 10712–10713.
[37] F. Su, J. Zeng, P. Bai, L. Lv, P.-Z. Guo, H. Sun, H.L. Li, J. Yu, J.Y. Lee, X.S. Zhao, Ind. Eng. Chem. Res. 46 (2007) 9097–9102.
[38] R. Fu, T.F. Baumann, S. Cronin, G. Dresselhaus, M.S. Dresselhaus, J.H. Satcher, Langmuir 21 (2005) 2647–2651.
[39] F. Su, X. Li, L. Lv, X.S. Zhao, Carbon 44 (2006) 801–803.
[40] F. Su, X.S. Zhao, Y. Wang, J.Y. Lee, Micropor. Mesopor. Mater. 98 (2007) 323–329.
[41] J.H. Zeng, J.Y. Lee, W.J. Zhou, J. Power Sources 159 (2006) 509–513.
[42] C. Wang, X. Pan, S. Guo, W. Chen, X. Bao, J. Mater. Chem. 18 (2008) 5782–5786.
[43] G. Zhang, D. Yang, E. Sacher, J. Phys. Chem. C 111 (2006) 565–570.
[44] Z. Liu, X. Lin, J.Y. Lee, W. Zhang, M. Han, L.M. Gan, Langmuir 18 (2002) 4054–4060.
[45] Z. Liu, J.Y. Lee, W. Chen, M. Han, L.M. Gan, Langmuir 20 (2004) 181–187.
[46] Y. Liang, H. Zhang, H. Zhong, X. Zhu, Z. Tian, D. Xu, B. Yi, J. Catal. 238 (2006) 468–476.
[47] A.S. Aricò, A.K. Shukla, H. Kim, S. Park, M. Min, V. Antonucci, Appl. Surf. Sci. 172 (2001) 33–40.
[48] D.Q. Yang, E. Sacher, J. Phys. Chem. C 112 (2008) 4075–4082.
[49] J. Solla-Gullón, P. Rodríguez, E. Herrero, A. Aldaz, J.M. Feliu, Phys. Chem. Chem. Phys. 10 (2008) 1359–1373.
[50] I. Kruusenberg, M. Marandi, V. Sammelselg, K. Tammeveski, Electrochem. Solid-State Lett. 12 (2009) F31–F34.